



# Engineering Pt single atom catalyst with abundant lattice oxygen by dual nanospace confinement strategy for the efficient catalytic elimination of VOCs

Weigao Han<sup>a,b,1</sup>, Weitong Ling<sup>d,1</sup>, Peng Gao<sup>e</sup>, Fang Dong<sup>a,c,\*</sup>, Zhicheng Tang<sup>a,\*</sup>

<sup>a</sup> National Engineering Research Centre for Fine Petrochemical Intermediates, State Key Laboratory for Oxo Synthesis and Selective Oxidation, Lanzhou Institute of Chemical Physics, Chinese Academy of Sciences, Lanzhou 730000, China

<sup>b</sup> University of Chinese Academy of Sciences, Beijing 100049, China

<sup>c</sup> Dalian National Laboratory for Clean Energy, Dalian 116023, China

<sup>d</sup> State Key Laboratory of Fine Chemicals and Key Laboratory of Industrial Ecology and Environmental Engineering, School of Environmental Science & Technology, Dalian University of Technology, Dalian 116024, China

<sup>e</sup> College of Chemistry & Chemical Engineering, Northwest Normal University, Lanzhou 730070, Gansu, China

## ARTICLE INFO

### Keywords:

Pt SACs

CeO<sub>2</sub>

In situ SERS

VOCs

Catalytic combustion

## ABSTRACT

Precisely constructing Pt single atom catalyst (SACs) with fine-tuned chemical environments is a vitally challenging issue, which has attracted peoples' attentions. The activation of lattice oxygen linked to active sites is also a great challenge to heterogeneous catalysis. Herein, via a cage-encapsulating strategy, Pt single atom (SA) was accurately constructed by dual nanospace confinement of three-dimensional ordered macroporous (3DOM) CeO<sub>2</sub> pore and Ce-MOFs nanocages. During calcination, CeO<sub>2</sub> derived from Ce-MOF restricted the migration of Pt SA and prevented its agglomeration. With the construction of CeO<sub>2</sub> nanocage, more active Pt-O<sub>2</sub> bond was created. More active lattice oxygen was linked to Pt single atom. DFT calculation also confirmed VOCs molecules were more easily absorbed on the catalyst surface and CO was more easily oxidized to CO<sub>2</sub>. The 90% conversion temperature (T<sub>90</sub>) of Pt<sub>1</sub>/CeO<sub>2</sub> @CeO<sub>2</sub>-0.2 (T<sub>90</sub> = 268 °C) was 81 °C lower than the T<sub>90</sub> of Pt<sub>1</sub>/CeO<sub>2</sub> (T<sub>90</sub> = 349 °C) on the catalytic combustion of benzene.

## 1. Introduction

Volatile organic compounds (VOCs) had great damage on the global environment and human health. Catalytic combustion was regarded as a promising technology to control the emission of VOCs. The noble catalyst has attracted more and more people's attention because of its excellent catalytic performance. But its high cost also limited its application. So it became very important to decrease the usage of the noble metal. Single atom catalysts were widely studied in the catalytic oxidation of VOCs because of its high catalytic performance and the maximum use of metal ions [1,2]. Wang et al. [3] prepared the Pd SACs with ZnMn<sub>2</sub>O<sub>4</sub> @MnO<sub>2</sub> support and the adsorbed oxygen and lattice oxygen were greatly improved. As a result of this, it achieved a good catalytic performance in the oxidation of CO and toluene. Su et al. [4]

prepared Pt-Co/HZSM-5 ternary catalysts and applied it in the catalytic oxidation of dichloromethane. And the preparation of Pt single atom increased the amount of oxygen vacancies on the surface of Co<sub>3</sub>O<sub>4</sub>. Based on these reports, it could be found that the oxygen activation played an important role in the catalytic oxidation of VOCs. The modification of SACs' coordination environment has attracted more and more peoples' attention. It also provided many possibilities to regulate the chemical properties. Bi et al. [5] modified Pd SA with Cl species and the Pd<sub>1</sub>-Cl species were formed during the calcination. This modification method generated more oxygen vacancies and more active oxygen.

Many modification methods were reported in the recent studies [6, 7]. The regulation of the coordination number was a common way to study the influence of coordination environment on the activity of single atom. And the coordination number could be easily changed by

\* Corresponding author at: National Engineering Research Centre for Fine Petrochemical Intermediates, State Key Laboratory for Oxo Synthesis and Selective Oxidation, Lanzhou Institute of Chemical Physics, Chinese Academy of Sciences, Lanzhou 730000, China.

\* Corresponding author.

E-mail addresses: [dongfang@licp.cas.cn](mailto:dongfang@licp.cas.cn) (F. Dong), [tangzhicheng@licp.cas.cn](mailto:tangzhicheng@licp.cas.cn) (Z. Tang).

<sup>1</sup> W.H. and W.L. contributed equally to this work.

changing the thermal activation temperature [8]. But this strategy was commonly used on M<sub>1</sub>-N-C catalysts. For metal oxide catalysts, the construction of double-atom catalysts (DACs) was an effective way to improve the catalytic performance. Hu et al. [9] anchored Ru<sub>1</sub> and Ni<sub>1</sub> two single atoms on the surface of CeO<sub>2</sub> and obtained the Ce<sub>0.95</sub>Ni<sub>0.025</sub>Ru<sub>0.025</sub>O<sub>2</sub> samples. The catalyst showed a high activity on the reforming methane with CO<sub>2</sub> to produce H<sub>2</sub> and CO. It also had a 98.5% selectivity of H<sub>2</sub>. The addition of other single atoms could efficiently improve the activity and selectivity. Now it has been increasing interest in using the pore-confined nanospaces of metal organic frameworks (MOFs) to modulate the microenvironment of SA. Su et al. [10] confined metal SA (M-SA) in the pore-confined nanospaces of porphyrinic MOFs and the M-SA was anchored on the Zr(IV)-oxo clusters through M–O/N bond. Jiang et al. [11] also encapsulated Au<sub>25</sub> nanoclusters (NCs) in UiO-66-X (X = H, NH<sub>2</sub>, OH, and NO<sub>2</sub>). The result turned out that the different surface ligands on UiO-66-X modulated the electronic state of Au<sub>25</sub> NCs and the adsorption energy of Au<sub>25</sub>@UiO-66-X to the support. Based on these reports, it could be found that the modifications of coordinating environment could effectively improve the catalytic activity of SACs. In this paper, we changed the coordination environment of Pt SA with a cage-encapsulating strategy. We encapsulated Pt SA in the pore-confined nanospace of MOFs.

After pyrolysis, MOFs could be converted to oxides. The core-shell structure not only confined the active sites but also provided a unique chemical environment. And the active sites might be trapped at the interface and certain chemical environments. It was found that the electronic states of the confined metal species are different from the bulks, which also lead a change on chemical properties. Bao et al. [12] confined the coordinatively unsaturated ferrous (CUF) in the matrices. The interface confinement could stable the CUF sites because of the interaction of metal and support. Benefitting from the modification of unsaturated low-valent active sites, the CUF sites and its adjacent metal atoms showed an excellent catalytic performance on CO oxidation. During the calcination, the active species might migrate and agglomerate. With the oxides layer, the oxides could capture the migrated ions and improve the dispersion of active species. Kim et al. [13] trapped precious metal species with a SiO<sub>2</sub> layer. Without the SiO<sub>2</sub> layer, it was found that the precious metal agglomerated to clusters. With the SiO<sub>2</sub> layer, it was found that the precious metal could maintain atomic dispersion. In this paper, we successfully confined Pt single atom with cerium oxides and controlled the thickness of the cage's growth. CeO<sub>2</sub> has plenty of oxygen vacancy, which could be used to stabilize the single atom [14]. It also had a strong metal-support interaction (MSI) and various electronic structures [15].

Herein, Pt SA was confined in the framework of 3DOM CeO<sub>2</sub> support first. Then a Ce-MOF layer was covered on the 3DOM CeO<sub>2</sub> support. In this way, each Pt SA could be guaranteed to be encapsulated in a nanocage of Ce-MOF. By precisely controlling the growth of Ce-MOF on the pore walls, the activity could be regulated. After calcination, CeO<sub>2</sub> derived from Ce-MOF could also restrict the migration of Pt SA and prevented its agglomeration. As a result of dual nanospace-confinement strategy, the coordinating environment of Pt SA was changed. More active Pt–O<sub>2</sub> interface was created. By precisely controlling the thickness of CeO<sub>2</sub> cage, the influence of CeO<sub>2</sub> cage on Pt SA was studied. Compared with Pt<sub>1</sub>/CeO<sub>2</sub>, the activity of the Pt<sub>1</sub>/CeO<sub>2</sub>@CeO<sub>2</sub>-0.2 samples had a significant increase. The T<sub>90</sub> of Pt<sub>1</sub>/CeO<sub>2</sub>@CeO<sub>2</sub>-0.2 (T<sub>90</sub> = 268 °C) was 81 °C lower than the T<sub>90</sub> of Pt<sub>1</sub>/CeO<sub>2</sub> (T<sub>90</sub> = 349 °C) on the catalytic combustion of benzene. This could be attributed to the enhancement of Pt–O<sub>2</sub> bond.

## 2. Experimental section

### 2.1. Catalyst preparation

#### 2.1.1. Preparation of highly ordered PMMA colloidal crystal template (CCT)

The preparation of PMMA microspheres was followed the reported methods [16]. The obtained PMMA emulsion was put into a centrifuge tub with a 3000 rpm. Then the highly ordered CCT was prepared.

#### 2.1.2. Preparation of 3DOM CeO<sub>2</sub>

0.75 g of P123, 1.05 g of citric acid, 2.17 g of Ce(NO<sub>3</sub>)<sub>2</sub>·6 H<sub>2</sub>O, 8 ml of ethanol and 2 ml of H<sub>2</sub>O were mixed together and stirred in a water bath with 60 °C for 4 h. Then the PMMA CCT was impregnated into the solution. A few minutes later, the solution was poured into the Buchner funnel. The filtrate was collected and poured into the Buchner funnel. This process repeated 3 times. The obtained PMMA was dried at 80 °C for 12 h. The dried samples were calcined in a tube furnace under an air atmosphere. The temperature was heated to 600 °C with a heating rate 2 °C/min and kept for 5 h. Finally, the 3DOM CeO<sub>2</sub> was prepared.

#### 2.1.3. Preparation of 3DOM Pt<sub>1</sub>/CeO<sub>2</sub>

The 0.3 wt% Pt<sub>1</sub>/CeO<sub>2</sub> SACs were prepared with a PVA-protected reduction methods. 0.039 ml of H<sub>2</sub>PtCl<sub>6</sub> (38.6 mmol/L) solution was mixed with PVA (Pt/PVA mass ratio = 1:1.2) in an ice bath with stirring. 0.1 g of 3DOM CeO<sub>2</sub> and 0.001 g of (NH<sub>4</sub>)<sub>2</sub>CO<sub>3</sub> were dispersed in methanol. The former was poured into the latter drop by drop. The mixed solution was stirred for 3 h. 0.01 g of NaBH<sub>4</sub> was dissolved in 2 ml of water. And then the NaBH<sub>4</sub> solution was added to the mixed solution drop by drop. After 1 h, the solution was filtered and dried at 60 °C for 12 h. The dried samples were calcined in muffle furnace. The temperature was heated to 550 °C with a heating rate 1 °C/min and kept for 2 h. Finally, the 0.3 wt% 3DOM Pt<sub>1</sub>/CeO<sub>2</sub> SACs was prepared. We called it Pt<sub>1</sub>/CeO<sub>2</sub>.

#### 2.1.4. Preparation of 3DOM Pt<sub>1</sub>/CeO<sub>2</sub>@CeO<sub>2</sub>-x

Pt<sub>1</sub>/CeO<sub>2</sub>@Ce-MOFs-0.02 was prepared with isovolume impregnation methods. 0.02 g of Ce(NO<sub>3</sub>)<sub>2</sub>·6 H<sub>2</sub>O was dissolved in methanol. The solution was poured into the dried 3DOM Pt<sub>1</sub>/CeO<sub>2</sub> samples. Then the samples was kept the vacuum at 2 MPa and dried at 80 °C. 0.05 g of benzenetricarboxylic acid and 0.009 g of CTAB was dissolved in 5 ml water and 5 ml methanol. The solution was poured into the dried samples and kept stirring for 6 h. Then the samples were collected by centrifugation and washed several times. After dried at 80 °C for 12 h, the Pt<sub>1</sub>/CeO<sub>2</sub>@Ce-MOFs-0.02 was obtained. The dried samples were calcined in muffle furnace. The temperature was heated to 550 °C with a heating rate 1 °C/min and kept for 2 h. Finally, the Pt<sub>1</sub>/CeO<sub>2</sub>@CeO<sub>2</sub>-0.02 was prepared. We called it Pt<sub>1</sub>/CeO<sub>2</sub>@CeO<sub>2</sub>-0.02. The Pt<sub>1</sub>/CeO<sub>2</sub>@CeO<sub>2</sub>-0.1, Pt<sub>1</sub>/CeO<sub>2</sub>@CeO<sub>2</sub>-0.2 and Pt<sub>1</sub>/CeO<sub>2</sub>@CeO<sub>2</sub>-0.4 was prepared by replacing 0.02 g of Ce(NO<sub>3</sub>)<sub>2</sub>·6 H<sub>2</sub>O with 0.1 g, 0.2 g and 0.4 g of Ce(NO<sub>3</sub>)<sub>2</sub>·6 H<sub>2</sub>O.

#### 2.1.5. Preparation of Pt<sub>1</sub>/CeO<sub>2</sub>-x-MOF

0.2 g of Ce(NO<sub>3</sub>)<sub>2</sub>·6 H<sub>2</sub>O was dissolved in methanol. We called it solution A. 0.05 g of benzenetricarboxylic acid was dissolved in 5 ml water and 5 ml methanol. We called it solution B. The solution A was poured into the solution B and kept stirring for 6 h. Then the samples were collected by centrifugation and washed several times. After dried at 80 °C for 12 h, Ce-MOFs was obtained. The dried samples were calcined in muffle furnace. The temperature was heated to 600 °C with a heating rate 2 °C/min and kept for 5 h. Finally, the CeO<sub>2</sub>-x-MOF was prepared. The 0.3 wt% Pt<sub>1</sub>/CeO<sub>2</sub>-x-MOF was prepared with the previous method.

## 2.2. Catalysts characterization

The catalysts were characterized by Scanning electron microscope (SEM), transmission electron microscopy (TEM), X-ray diffraction (XRD), N<sub>2</sub> adsorption-desorption, H<sub>2</sub> temperature-programmed reduction (H<sub>2</sub>-TPR), oxygen temperature programmed desorption (O<sub>2</sub>-TPD), ammonia temperature programmed desorption (NH<sub>3</sub>-TPD), X-ray photoelectron spectroscopy (XPS), diffuse reflectance Fourier-transform infrared (DRIFT) spectroscopy, and X-ray absorption near-edge spectra (XANES). The detailed characterization procedures were described in [Supplementary Material](#).

## 2.3. Catalytic activity tests

The catalytic oxidation of toluene was evaluated by using a fixed-bed flow reactor operating at steady-state flow mode. Then, 0.4 g catalysts

(40–60 mesh) and 0.7 g quartz sand (40–60 mesh) were mixed uniformly. They were put onto the reactor. The reaction gas containing VOCs (3000 ppm) was generated by bubbling air through a VOC saturator, and then passed through the reactor with a weight hourly space velocity (WHSV) of 30000 ml g<sup>-1</sup> h<sup>-1</sup>. The first temperature was 100 °C. The activity was measured per 20 °C. Before each test, it needed to stabilize for 1 h. Reactants and products were analyzed with an online GC-6820 gas chromatograph with a flame ionization detector. Conversion was defined as:

$$C_{\text{toluene}} = \frac{[C]_{\text{inlet}} - [C]_{\text{outlet}}}{[C]_{\text{inlet}}} \times 100\%$$

The catalytic oxidation of toluene was evaluated by using a fixed-bed flow reactor operating at steady-state flow mode. Then, 0.2 g catalysts (40–60 mesh) and 0.4 g quartz sand (40–60 mesh) were mixed uniformly. They were put onto the reactor. The reaction gas containing

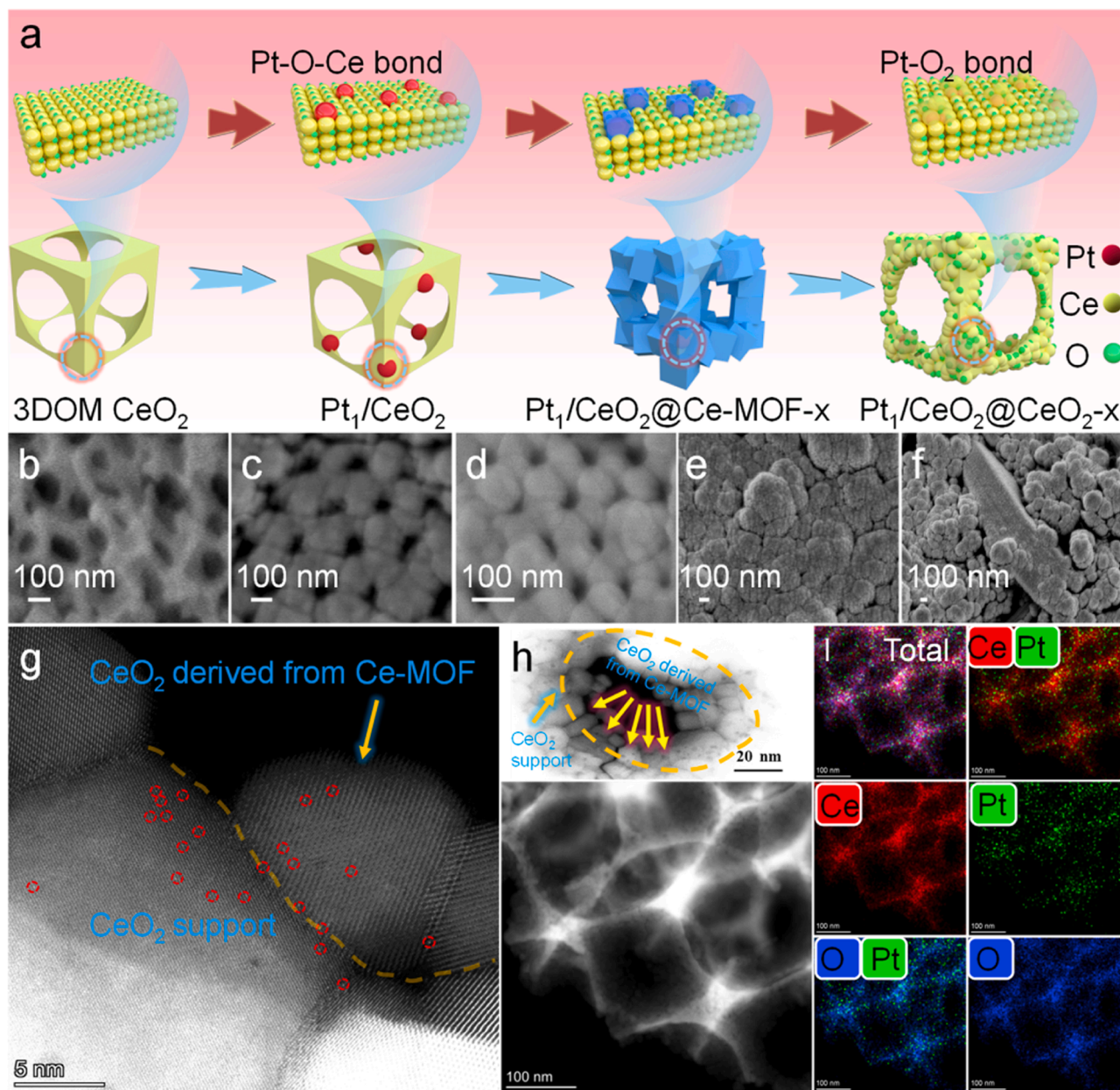


**Fig. 1.** (a) Preparation of the Pt<sub>1</sub>/CeO<sub>2</sub> @CeO<sub>2</sub>-x samples. The SEM images of Pt<sub>1</sub>/CeO<sub>2</sub> (b), Pt<sub>1</sub>/CeO<sub>2</sub> @Ce-MOF-0.02 (c), Pt<sub>1</sub>/CeO<sub>2</sub> @Ce-MOF-0.1 (d), Pt<sub>1</sub>/CeO<sub>2</sub> @Ce-MOF-0.2 (e), and Pt<sub>1</sub>/CeO<sub>2</sub> @Ce-MOF-0.4 (f). The AC-HAADF-STEM image of Pt<sub>1</sub>/CeO<sub>2</sub> @CeO<sub>2</sub>-0.1 samples (g) (h). The energy-dispersive X-ray spectroscopy of Pt<sub>1</sub>/CeO<sub>2</sub> @CeO<sub>2</sub>-0.1 samples (i).



VOCs (2000 ppm) was generated by bubbling air through a VOC saturator, and then passed through the reactor with a weight hourly space velocity (WHSV) of  $60000 \text{ ml g}^{-1} \text{ h}^{-1}$ . The first temperature was  $100^\circ\text{C}$ . The activity was measured per  $20^\circ\text{C}$ . Before each test, it needed to stabilize for 1 h. Reactants and products were analyzed with an online GC-6820 gas chromatograph with a flame ionization detector. Conversion was defined as:

$$C_{\text{benzene}} = \frac{[C]_{\text{inlet}} - [C]_{\text{outlet}}}{[C]_{\text{inlet}}} \times 100\%$$

Further details could be found in [Supplementary Material](#).

### 3. Results and discussion

#### 3.1. Construction and morphological characterization of 3DOM Pt<sub>1</sub>/CeO<sub>2</sub>@CeO<sub>2</sub>-x samples

As shown in Fig. 1a, Pt SACs was prepared with a reported method first [17]. The loading of Pt species was 0.3 wt% over the Pt<sub>1</sub>/CeO<sub>2</sub> samples. And 3DOM Pt<sub>1</sub>/CeO<sub>2</sub> was used to provide growth sites for the growth of Ce-MOFs. In this way, Pt SA could be guaranteed to confine in the nanospace of Ce-MOF. By varying the amount of absorbed Ce salt, the cages' thickness of Ce-MOFs on 3DOM CeO<sub>2</sub> support was controlled. Then the Pt<sub>1</sub>/CeO<sub>2</sub> @Ce-MOF-x was prepared. After a process of calcination, the Pt<sub>1</sub>/CeO<sub>2</sub> @CeO<sub>2</sub>-x was obtained. So the Pt SA was confined in the cage of CeO<sub>2</sub>. X was presented as the amount of the absorbed Ce salt. In the preparation process, Pt SA was confined into the framework of 3DOM CeO<sub>2</sub> through oxygen vacancies first. Because of the high surface free energy of SA, Pt atoms tended to aggregate. To avoid this, Ce-MOF grew on the framework of 3DOM CeO<sub>2</sub>. In this way, Ce-MOF acted as a nanocage to hold Pt atoms in the pore of Ce-MOF. During the calcination process, the oxygen vacancies derived from Ce-MOF could also capture the migrated Pt atoms. And the nanocage of CeO<sub>2</sub> could also act as the shell to wrap the core of Pt atoms. In this way, the thickness of shell could influence the expression of the core and more active interface could be created.

The bonding form and electron density of Pt SA was changed by regulating the thickness of CeO<sub>2</sub>. The pore size was used to evaluate the thickness of cerium oxides. As shown in Fig. 1b, it could be seen that the pore size of 3DOM Pt<sub>1</sub>/CeO<sub>2</sub> was 250 nm. When the cage of Ce-MOF was constructed, the pore size of Pt<sub>1</sub>/CeO<sub>2</sub> @Ce-MOF-0.1 was 50 nm (Fig. 1c). It illustrated that Ce-MOF was successfully grown on the pores of Pt<sub>1</sub>/CeO<sub>2</sub>. With the content of Ce increasing, the pore size of 3DOM CeO<sub>2</sub> was totally blocked with Ce-MOF in the Pt<sub>1</sub>/CeO<sub>2</sub> @Ce-MOF-0.2 samples (Fig. 1d). In the Pt<sub>1</sub>/CeO<sub>2</sub> @Ce-MOF-0.4 samples (Fig. 1e), the pore was blocked and some rod-like Ce-MOF also formed. This illustrated that the pore had a maximum capacity. The excess Ce salt could form rod-like structures. According to the TEM images, all samples maintained the 3DOM structure (Fig. S1). And the pore size also had an obvious change. The pore size of 3DOM Pt<sub>1</sub>/CeO<sub>2</sub> was about 250 nm (Fig. S1b), which was the same with SEM image. The pore size of Pt<sub>1</sub>/CeO<sub>2</sub> @CeO<sub>2</sub>-0.02 was about 200 nm (Fig. S1c). With the content of Ce increasing, the pore size didn't change anymore. The pore size of 3DOM Pt<sub>1</sub>/CeO<sub>2</sub> @CeO<sub>2</sub>-0.1 and 3DOM Pt<sub>1</sub>/CeO<sub>2</sub> @CeO<sub>2</sub>-0.2 were about 100 nm (Fig. S1d and Fig. S1e). When the content of Ce increased further, some rod-like structure also appeared (Fig. S1f). Aberration-corrected high-angle annular dark-field scanning transmission electron microscopy (AC-HAADF-STEM) image showed the dispersion of Pt species on the 3DOM Pt<sub>1</sub>/CeO<sub>2</sub> @CeO<sub>2</sub>-0.1 samples. It could be found that Pt species were atomically dispersed on the CeO<sub>2</sub> support. As shown in Fig. 1g and Fig. S2, the bright dots under the HAADF-STEM mode were Pt SA. From the elemental mapping images by energy-dispersive X-ray spectroscopy (EDS), it could be confirmed that Pt atoms had atomic dispersion (Fig. 1h). Interestingly, it was found that some Pt SA migrated into the CeO<sub>2</sub> derived from Ce-MOF.

#### 3.2. The characterization of Pt single atom (SA) confined into dual Nanospace

The coordinating environment of Pt SA was identified by the X-ray absorption near-edge structure (XANES) spectra (Fig. 2a and b). The adsorption energy at 11567.66 eV in the XANES spectra of Pt SACs was similar to that of PtO<sub>2</sub>, suggesting that Pt-O bond was the dominating species on the Pt<sub>1</sub>/CeO<sub>2</sub> @CeO<sub>2</sub>-0.1 samples [18,19]. As shown in Fig. 2c, atomically dispersed Pt on the Pt<sub>1</sub>/CeO<sub>2</sub> @CeO<sub>2</sub>-0.1 samples showed a prominent peak around 1.61 Å, representing the Pt-O bond. And the Pt-Pt bond (ca 2.62 Å) over Pt<sub>1</sub>/CeO<sub>2</sub> @CeO<sub>2</sub>-0.1 at higher R was absent. To explore the atomic dispersion of Pt on Pt<sub>1</sub>/CeO<sub>2</sub> @CeO<sub>2</sub>-0.1 samples, wavelet transform (WT) of Pt K-edge EXAFS was carried out. In Fig. 2d, the WT contour plots of Pt SA show two intensity maximum at 3.64 and 5.62 Å. This could be regarded as PtO<sub>2</sub>. Compared with the WT plot of Pt foil, no intensity maximum related Pt-Pt bond could be found. Other EXAFS analysis and the fitting results were shown in Fig. S3 and Table S1. According the fitting result, Pt existed mainly in the form of Pt-O and Pt-O-Ce bond (Fig. 2d and S3). This illustrated that the Pt SA was the main species on the samples, verifying that the Pt SACs was successfully prepared. The in situ SERS result could also illustrate the formation of Pt SA. The incomplete combustion of VOCs might generate CO molecules. According to in situ SERS results, peaks at 1780 and 2060 cm<sup>-1</sup> could be considered as the C-O stretching mode of CO adsorbed on the bridge site ( $\nu(\text{C-O})_{\text{bridge}}$ ) and top site ( $\nu(\text{C-O})_{\text{top}}$ ), respectively. As shown in Fig. 2e and f, the Pt<sub>1</sub>/CeO<sub>2</sub> samples showed a relatively strong bridge adsorption peak and a strong top adsorption peak. But the Pt<sub>1</sub>/CeO<sub>2</sub> @CeO<sub>2</sub>-0.1 samples showed a strong top adsorption peak. It indicated that Pt SA tended to agglomerate over the Pt<sub>1</sub>/CeO<sub>2</sub> samples during the calcination. With the cage-encapsulating strategy, the Pt atoms over the Pt<sub>1</sub>/CeO<sub>2</sub> @CeO<sub>2</sub>-0.1 samples didn't agglomerate and CeO<sub>2</sub> derived from Ce-MOF could capture the migrated Pt SA during the calcination. With the temperature increasing, the  $\nu(\text{C-O})_{\text{top}}$  disappeared gradually [20,21]. It indicated that CO was easy to be desorbed and converted on the Pt<sub>1</sub>/CeO<sub>2</sub> @CeO<sub>2</sub>-0.1 samples. There was no obvious change on the Pt<sub>1</sub>/CeO<sub>2</sub> samples. This might be caused that Pt SA had a high free energy and Pt SA tended agglomeration during the calcination. The CeO<sub>2</sub> nanocage derived from Ce-MOF could generate plenty of oxygen vacancy during calcination. Then CeO<sub>2</sub> could restrict the migration of Pt SA and avoid the generation of Pt cluster. So the construction of CeO<sub>2</sub> nanocage could improve the dispersion of Pt species.

#### 3.3. Catalytic performance and redox ability

The catalytic performance of all samples was evaluated under three conditions: toluene, benzene and benzene/SO<sub>2</sub>. As shown in Fig. 3a and b, the 3DOM Pt<sub>1</sub>/CeO<sub>2</sub> showed a poor catalytic performance compared with the confined catalyst. The T<sub>90</sub> (the temperatures for 90% VOCs conversion) was  $347^\circ\text{C}$ . After Pt SA was encapsulated in CeO<sub>2</sub>, the catalytic performance of Pt<sub>1</sub>/CeO<sub>2</sub> @CeO<sub>2</sub>-0.2 catalysts had a significant improvement, whose T<sub>90</sub> was  $287^\circ\text{C}$ . The T<sub>90</sub> has been reduced by  $60^\circ\text{C}$ . To confirm the confined effect, the Pt<sub>1</sub>/CeO<sub>2</sub> catalyst mechanically mixed with pure CeO<sub>2</sub> powder was tested. The result showed that the mixed Pt<sub>1</sub>/CeO<sub>2</sub> and CeO<sub>2</sub> showed a poor performance, in which T<sub>90</sub> was  $353^\circ\text{C}$ . It illustrated that this confined catalyst achieved good results. To study the influence of cage's thickness on catalytic activity, different content of Ce was added to build the cage. The activity showed that Pt<sub>1</sub>/CeO<sub>2</sub> @CeO<sub>2</sub>-0.2 > Pt<sub>1</sub>/CeO<sub>2</sub> @CeO<sub>2</sub>-0.1 > Pt<sub>1</sub>/CeO<sub>2</sub> @CeO<sub>2</sub>-0.02 > Pt<sub>1</sub>/CeO<sub>2</sub> @CeO<sub>2</sub>-0.4 > Pt<sub>1</sub>/CeO<sub>2</sub>. The catalytic performance tested under benzene conditions also followed this order. The T<sub>90</sub> of Pt<sub>1</sub>/CeO<sub>2</sub> samples were  $349^\circ\text{C}$ , and the T<sub>90</sub> of Pt<sub>1</sub>/CeO<sub>2</sub> @CeO<sub>2</sub>-0.02 samples was  $268^\circ\text{C}$ . The T<sub>90</sub> of Pt<sub>1</sub>/CeO<sub>2</sub> @CeO<sub>2</sub>-0.2 was  $81^\circ\text{C}$  lower than the T<sub>90</sub> of Pt<sub>1</sub>/CeO<sub>2</sub>. The activity had a significant increase. It illustrated that the thickness of CeO<sub>2</sub> cage had a big influence on the catalytic combustion of benzene. The catalytic performance of the Pt<sub>1</sub>/CeO<sub>2</sub>-x



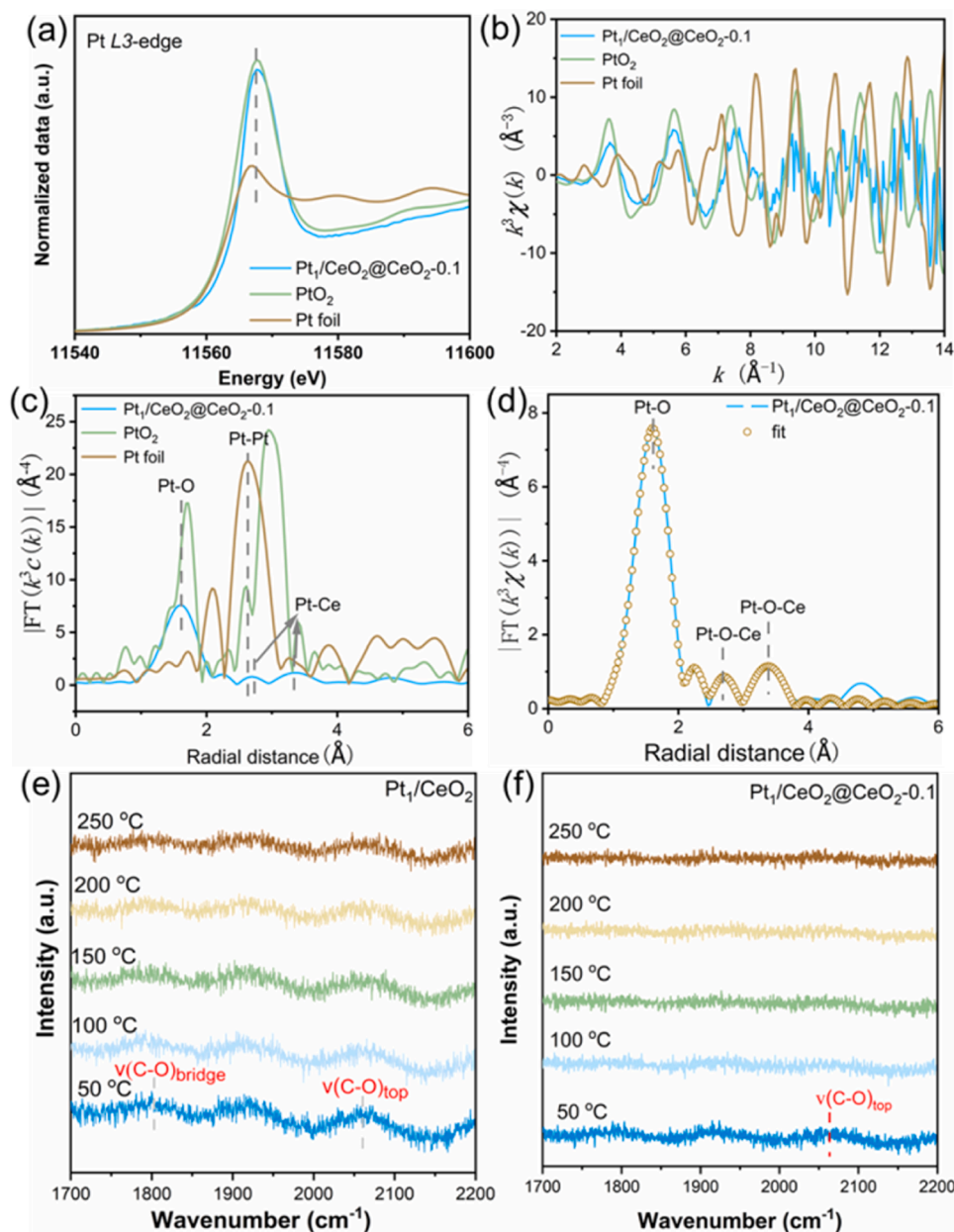


**Fig. 2.** (a) Normalized XANES for  $\text{Pt}_1/\text{CeO}_2 @\text{CeO}_2\text{-}0.1$  samples at the Pt-L3 edge (b) Pt K-edge of near-edge XANES spectra for of  $\text{Pt}_1/\text{CeO}_2 @\text{CeO}_2\text{-}0.1$  samples, (c) EXAFS magnitude of the Fourier transformed  $k^2$ -weighted  $\chi(k)$  data for of  $\text{Pt}_1/\text{CeO}_2 @\text{CeO}_2\text{-}0.1$  samples, (d) the fitted EXAFS magnitude of the Fourier transformed  $k^2$ -weighted  $\chi(k)$  data for of  $\text{Pt}_1/\text{CeO}_2 @\text{CeO}_2\text{-}0.1$  samples, (e) In situ SERS of benzene adsorption at different temperatures over  $\text{Pt}_1/\text{CeO}_2$ , (f) In situ SERS of benzene adsorption at different temperatures over  $\text{Pt}_1/\text{CeO}_2 @\text{CeO}_2\text{-}0.1$  samples.

MOF samples was also tested. According to the activity test, it was found that  $\text{Pt}_1/\text{CeO}_2\text{-}x\text{-MOF}$  showed a good catalytic performance (Fig. 3b). This might be caused that  $\text{CeO}_2\text{-}x$  derived from Ce-MOF was more favorable. The catalytic performance of  $\text{Pt}_1/\text{CeO}_2\text{-}x\text{-MOF}$  was poor than the  $\text{Pt}_1/\text{CeO}_2 @\text{CeO}_2\text{-}0.2$  samples. This might be caused that Pt SAs were confined into the dual nanospace of 3DOM  $\text{CeO}_2$  support and  $\text{CeO}_2$  nanocage derived from Ce-MOF. As a result of this, the  $\text{Pt}_1/\text{CeO}_2 @\text{CeO}_2\text{-}0.2$  samples had stronger metal-support interaction. But the activity of  $\text{Pt}_1/\text{CeO}_2\text{-}x\text{-MOF}$  was better than the  $\text{Pt}_1/\text{CeO}_2 @\text{CeO}_2\text{-}0.4$  samples. This might be caused that a thick  $\text{CeO}_2$  shell did influence the expression of Pt core. The sulfur resistance was also tested under the benzene/ $\text{SO}_2$  condition (Fig. 3c). The activity of  $\text{Pt}_1/\text{CeO}_2$  had a significant increase when the flow of  $\text{SO}_2$  was added. As the cage got thicker,  $\text{Pt}_1/\text{CeO}_2 @\text{CeO}_2\text{-}x$  samples showed a poor sulfur resistance. The total conversion temperature had a significant delay. The activity of

$\text{Pt}_1/\text{CeO}_2 @\text{CeO}_2\text{-}0.4$  samples even had a decrease when the temperature increased further. Fig. S6b showed the S 2p spectrum of the used  $\text{Pt}_1/\text{CeO}_2$  and  $\text{Pt}_1/\text{CeO}_2 @\text{CeO}_2\text{-}0.1$  samples. It could be found that a photoelectron line appeared at 168.6 eV over the  $\text{Pt}_1/\text{CeO}_2 @\text{CeO}_2\text{-}0.1$  samples. While in the  $\text{Pt}_1/\text{CeO}_2$  samples, the photoelectron line at 168.6 eV couldn't be found. It implied that  $\text{SO}_2$  molecules were more easily to absorb on the  $\text{Pt}_1/\text{CeO}_2 @\text{CeO}_2\text{-}0.1$  samples and the absorbed  $\text{SO}_2$  was oxidized to  $\text{SO}_4^{2-}$ . This might be caused that the  $\text{Pt}_1/\text{CeO}_2 @\text{CeO}_2\text{-}0.1$  samples had more active oxygen. The adsorption of  $\text{SO}_2$  consumed the active oxygen species. As a result of this, the activity of the  $\text{Pt}_1/\text{CeO}_2 @\text{CeO}_2\text{-}0.1$  samples decreased [22,23].

The water resistance was also tested on  $\text{Pt}_1/\text{CeO}_2$  and  $\text{Pt}_1/\text{CeO}_2 @\text{CeO}_2\text{-}0.1$  samples. The result showed that both samples showed a good water resistance and the nanocage didn't influence the water resistance (Fig. 3i). The  $\text{Pt}_1/\text{CeO}_2 @\text{CeO}_2\text{-}0.1$  samples also showed a

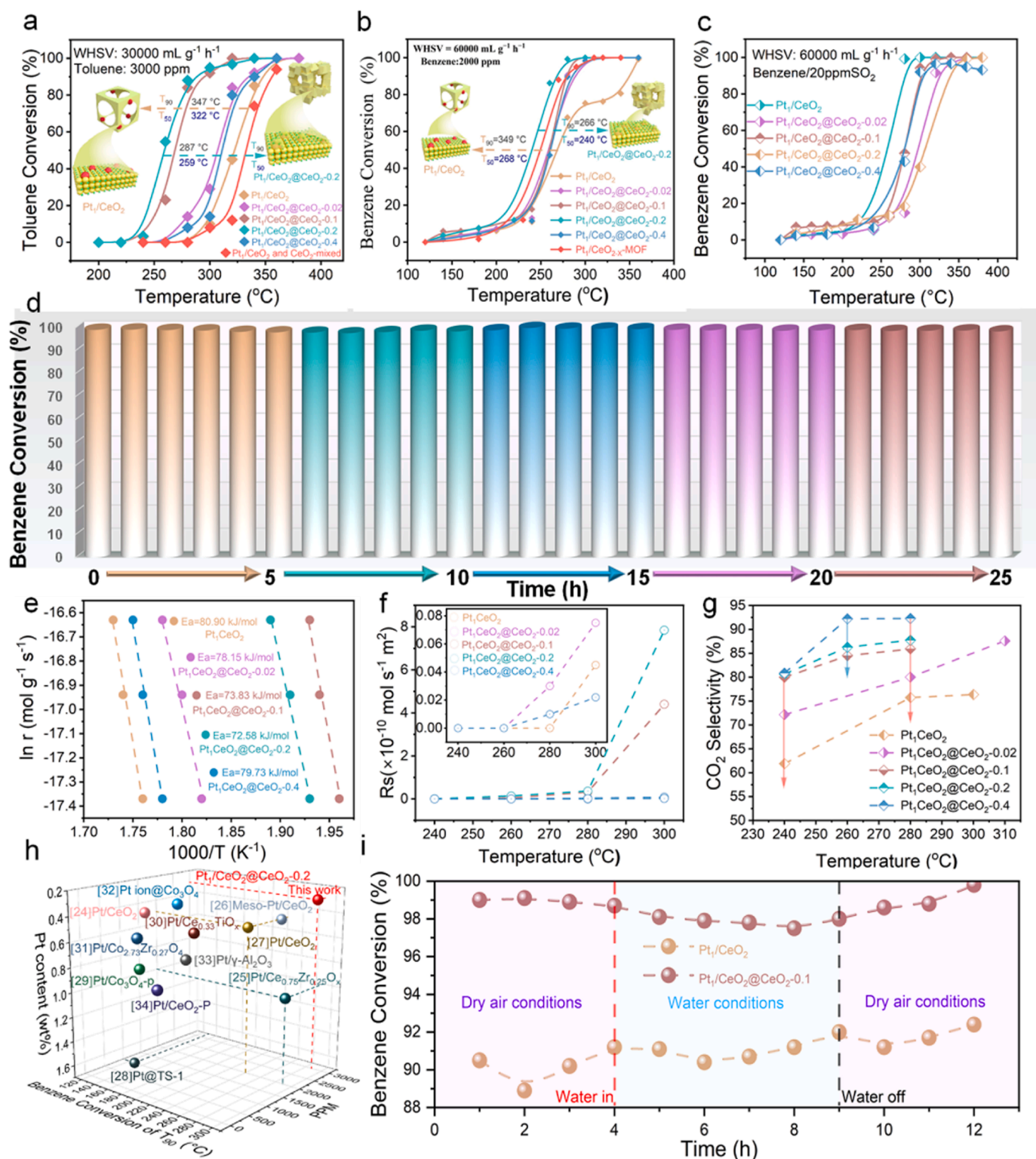


**Fig. 3.** Catalytic performance for toluene oxidation (a), benzene oxidation (b), and benzene+SO<sub>2</sub> (c), the CO<sub>2</sub> selectivity image (d), the water tolerance (e) and the thermal stability tests (f), the reaction rates (g), the comparison of active properties with other literatures (h), the Arrhenius plots of benzene catalytic combustion reaction over all samples (i).

long thermal stability (Fig. 3d). According to the slopes of Arrhenius plots (Fig. 3e), it followed this order: Pt<sub>1</sub>/CeO<sub>2</sub>@CeO<sub>2</sub>-0.2 (72.58 kJ mol<sup>-1</sup>) < Pt<sub>1</sub>/CeO<sub>2</sub>@CeO<sub>2</sub>-0.1 (73.83 kJ mol<sup>-1</sup>) < Pt<sub>1</sub>/CeO<sub>2</sub>@CeO<sub>2</sub>-0.02 (78.15 kJ mol<sup>-1</sup>) < Pt<sub>1</sub>/CeO<sub>2</sub>@CeO<sub>2</sub>-0.4 (79.73 kJ mol<sup>-1</sup>) < Pt<sub>1</sub>/CeO<sub>2</sub> (80.90 kJ mol<sup>-1</sup>). The surface reaction rate  $R_s$  were calculated and used to evaluate the conversion efficiency of VOCs (Fig. 3f).

The  $R_s$  values of all samples are: Pt<sub>1</sub>/CeO<sub>2</sub>@CeO<sub>2</sub>-0.2 > Pt<sub>1</sub>/CeO<sub>2</sub>@CeO<sub>2</sub>-0.1 > Pt<sub>1</sub>/CeO<sub>2</sub>@CeO<sub>2</sub>-0.02 > Pt<sub>1</sub>/CeO<sub>2</sub>@CeO<sub>2</sub>-0.4 > Pt<sub>1</sub>/CeO<sub>2</sub>. Fig. 3h showed the comparison of active properties with other literatures. Based on other literatures [24–34], it could be found that most of Pt-based catalysts were focused on the loading of Pt, oxygen species, confinement, and so on. Some of them use the other elements

such as Ir, Co, and Al to change the coordination environment and dispersion of Pt [24,25,29–32]. Some of them studied the influence of Pt's confinement on the oxidation of toluene [26–28]. And some of them studied the chemical properties of the carrier on the oxidation of toluene [33,34]. This work took full advantage of a low loading noble metal through a dual nanospace confinement strategy. And the Pt<sub>1</sub>/CeO<sub>2</sub>@CeO<sub>2</sub>-0.2 samples exhibited outstanding activity on the high concentration of toluene atmosphere.

As shown in Fig. S4, there were two peaks (531 and 808 °C) in pure 3DOM CeO<sub>2</sub> support [35,36]. The former was attributed to the reduction of Ce<sup>4+</sup> to Ce<sup>3+</sup> and the elimination of the absorbed oxygen species. The latter was attributed to the reduction of Ce<sup>4+</sup> to Ce<sup>3+</sup> and the elimination of the lattice oxygen species. With the loading of Pt, the reduction peaks shifted to a higher temperature (Pt<sub>1</sub>/CeO<sub>2</sub>). It also proved the formation of Pt SA as Pt single atoms were reduced at much high temperatures. With the construction of CeO<sub>2</sub> cage, the reduction peaks shifted to a low temperature. The reduction peaks of the Pt<sub>1</sub>/CeO<sub>2</sub>@CeO<sub>2</sub>-0.02 samples appeared around 36 and 277 °C. It illustrated that the construction of CeO<sub>2</sub> cage led a more active Pt-O bond and better reduction ability. With the cage thicker, the Pt<sub>1</sub>/CeO<sub>2</sub>@CeO<sub>2</sub>-0.1 samples showed an earlier peak at 241 °C. The Pt-O bond was activated further, which illustrated that Pt SA was tuned with O species. With the cage thicker and thicker, peaks around 241 °C shifted to a high temperature. The Pt<sub>1</sub>/CeO<sub>2</sub>@CeO<sub>2</sub>-0.4 samples showed a relatively high reduction peak at 302 °C. This illustrated that the thickness of CeO<sub>2</sub> cage influenced the expression of Pt-O bond. Above all, the introduction of Pt SA improved the reduction ability. It meant that the addition of cage activated the lattice oxygen of Pt SA. With the cage thicker, the reduction ability gradually weakened. It meant the proper amount was beneficial for the improvement of catalytic performance.

### 3.4. Surface chemical environment, texture and chemical property analysis

In situ surface enhanced Raman spectroscopy (SERS) was used to detect the bond vibration and the intermediates of the reaction. As shown in Fig. 4a, peaks at 462.1 cm<sup>-1</sup> and 656 cm<sup>-1</sup> could be attributed to the vibration of Ce-O (F<sub>2g</sub>) and Pt-O bond, respectively [37,38]. Compared with the Pt<sub>1</sub>/CeO<sub>2</sub> samples, the Pt<sub>1</sub>/CeO<sub>2</sub>@CeO<sub>2</sub>-0.1 samples also showed other peaks at 254 cm<sup>-1</sup> and 830 cm<sup>-1</sup>, which could be attributed to Pt-O<sub>2</sub> and O-O bond, respectively. Combined with other reports [15], it could be convinced that the peroxo or superoxo species were formed. Compared with the Pt<sub>1</sub>/CeO<sub>2</sub> samples, the Pt<sub>1</sub>/CeO<sub>2</sub>@CeO<sub>2</sub>-0.1 samples showed stronger O-O band. The formation of Pt-O<sub>2</sub> could illustrate that the coordination environment of Pt was changed. In the Pt<sub>1</sub>/CeO<sub>2</sub> samples, Pt mainly existed in the form of Pt-O bond. While in the Pt<sub>1</sub>/CeO<sub>2</sub>@CeO<sub>2</sub>-0.1 samples, Pt mainly existed in the form of Pt-O<sub>2</sub> bond. With the temperature increasing, the Ce-O bond shifted to a lower wavenumbers (Fig. 4a and b) and the stretching vibrations of Pt-O<sub>2</sub> bond enhanced (Fig. 4b). It meant that the Pt-O and Ce-O bond was activated during the reaction process.

Peaks at 563–595 cm<sup>-1</sup> were usually regarded as the defect-induced (D) vibration of oxygen vacancies (Ce-O<sub>v</sub>). Both Pt<sub>1</sub>/CeO<sub>2</sub> and Pt<sub>1</sub>/CeO<sub>2</sub>@CeO<sub>2</sub>-0.1 samples showed the Ce-O<sub>v</sub> bond. The intensity of Ce-O<sub>v</sub> bond over Pt<sub>1</sub>/CeO<sub>2</sub>@CeO<sub>2</sub>-0.1 samples was stronger than that of Pt<sub>1</sub>/CeO<sub>2</sub> samples. As shown in Fig. 4d and e, the Ce-O<sub>v</sub> bond in the Pt<sub>1</sub>/CeO<sub>2</sub>@CeO<sub>2</sub>-0.1 samples had an obvious red shift ( $\Delta = 10$  cm<sup>-1</sup>) with longer reaction times [39,40]. The Pt-O bond had a slight red shift and gradually weakened. But the Ce-O bond had no shift. Similar to this, the Ce-O<sub>v</sub> bond in the Pt<sub>1</sub>/CeO<sub>2</sub> samples also had a red shift ( $\Delta = 6$  cm<sup>-1</sup>). The Pt-O bond gradually weakened and the Ce-O bond had no change. This might illustrated that Pt-O and Ce-O<sub>v</sub> species acted as the adsorption sites for benzene. The Ce-O species wasn't helpful for the adsorption for benzene. It illustrated that the introduction of Pt species could effectively improve the adsorption ability of VOCs over CeO<sub>2</sub> support.

Based on the Hooke's law, the bond force constant (k) was positively

correlated to the Raman shift ( $\omega$ ). In the following equation, c represented the light velocity and  $\mu$  represented the effective mass. The lower the Raman shift is, the longer bond and the lower strength is.

$$\omega = \frac{\sqrt{k/\mu}}{2\pi c}$$

Compared with Pt<sub>1</sub>/CeO<sub>2</sub> samples ( $\Delta = 6$  cm<sup>-1</sup>), the Ce-O<sub>v</sub> bond in the Pt<sub>1</sub>/CeO<sub>2</sub>@CeO<sub>2</sub>-0.1 samples had an obvious red shift ( $\Delta = 10$  cm<sup>-1</sup>). It illustrated that the Pt<sub>1</sub>/CeO<sub>2</sub>@CeO<sub>2</sub>-0.1 samples had better adsorption capacity and activation of benzene. As shown in Fig. 4d and e, the Ce-O bond of Pt<sub>1</sub>/CeO<sub>2</sub> samples appeared at 461.70 cm<sup>-1</sup> and the Ce-O bond of Pt<sub>1</sub>/CeO<sub>2</sub>@CeO<sub>2</sub>-0.1 samples were mainly at 459.94 cm<sup>-1</sup>. The intensity of the Ce-O bond of all samples was also studied according to the Hooke's law. It could be found that the Pt<sub>1</sub>/CeO<sub>2</sub>@CeO<sub>2</sub>-0.1 samples had a smaller value of k. It illustrated that the Ce-O bond on the surface of Pt<sub>1</sub>/CeO<sub>2</sub>@CeO<sub>2</sub>-0.1 samples was easily broken. The intensity ratio of D peaks and F<sub>2g</sub> peaks ( $I_D/I_{2g}$ ) was calculated according to the In situ SERS. The  $I_D/I_{2g}$  was used to evaluate the concentration of oxygen vacancies (Fig. 4c). It was found that the concentration of oxygen vacancies increased with the temperature increasing. This illustrated that the oxygen species were activated with the temperature increasing and it was consumed during the reaction. As a result, more vacancies were formed. The Pt<sub>1</sub>/CeO<sub>2</sub>@CeO<sub>2</sub>-0.1 samples also had a higher concentration of oxygen vacancies than the Pt<sub>1</sub>/CeO<sub>2</sub> samples. This illustrated that the oxygen species were easy to be activated over the Pt<sub>1</sub>/CeO<sub>2</sub>@CeO<sub>2</sub>-0.1 samples and the Pt<sub>1</sub>/CeO<sub>2</sub>@CeO<sub>2</sub>-0.1 samples had better oxygen mobility.

Fig. S8 showed the NH<sub>3</sub>-TPD result. The percentage of surface acid sites was shown in Table S4. The CeO<sub>2</sub> support showed abundant weak and medium-strong acid sites (47.54%). After the introduction of Pt, the Pt<sub>1</sub>/CeO<sub>2</sub> samples showed plenty of strong acid sites (77.99%), which was not beneficial for the adsorption of VOCs. This might illustrate why the Pt<sub>1</sub>/CeO<sub>2</sub> samples showed a poor catalytic performance. After the Pt SA was encapsulated by CeO<sub>2</sub>, the weak acid sites of the Pt<sub>1</sub>/CeO<sub>2</sub>@CeO<sub>2</sub>-0.02 samples increased to 48.75%. With the cage thicker and thicker, the proportion of weak acid sites is increasing. It meant that the cage-encapsulating strategy could effectively improve the surface acidity of SACs. This would be beneficial for the adsorption and conversion of VOCs on the catalysts' surface, which was further studied by DFT. The specific surface area and pore volume were shown in Fig. S9 and Table S2. With the construction of CeO<sub>2</sub> nanocage, the specific surface area gradually increased. It provided more area for contact with the reactant molecules.

According to the XRD result (Fig. 4f), it could be found that both Pt<sub>1</sub>/CeO<sub>2</sub> and Pt<sub>1</sub>/CeO<sub>2</sub>@CeO<sub>2</sub>-0.2 samples mainly exposed the (111) lattice plane. So the adsorption energy of C<sub>6</sub>H<sub>6</sub> were calculated based on the (111) lattice plane. The C-C bond length, C-H bond length, and C-C-H bond angle for C<sub>6</sub>H<sub>6</sub> were optimized to be 1.396 Å, 1.039 Å, and 120.00°, respectively (Fig. S7). This model tended to the most stable state for this system. According to the DFT result (Fig. 4g), the bond length of Pt-H changed from 1.304 Å to 3.426 Å, when C<sub>6</sub>H<sub>6</sub> was absorbed on the Pt<sub>1</sub>/CeO<sub>2</sub> samples. The C-C-H bond angle changed from 120.00° to 120.266°. There was an obvious change in bond length of Ce-H from 1.429 Å to 4.009 Å, when C<sub>6</sub>H<sub>6</sub> was absorbed on the Pt<sub>1</sub>/CeO<sub>2</sub>@CeO<sub>2</sub> samples. The C-C-H bond angle changed from 120.00° to 120.232°. This might illustrated that C<sub>6</sub>H<sub>6</sub> was activated when C<sub>6</sub>H<sub>6</sub> was absorbed on the Pt<sub>1</sub>/CeO<sub>2</sub> and Pt<sub>1</sub>/CeO<sub>2</sub>@CeO<sub>2</sub> samples. Compared with Pt<sub>1</sub>/CeO<sub>2</sub> samples, C<sub>6</sub>H<sub>6</sub> was easier to absorb on the Pt<sub>1</sub>/CeO<sub>2</sub>@CeO<sub>2</sub> samples. Its adsorption energy was 1.524 eV, which turned out that the construction of confined catalyst was beneficial for the adsorption and activation of VOCs. Based on the DFT calculation, it could also found that the Pt<sub>1</sub>/CeO<sub>2</sub>@CeO<sub>2</sub> samples had a lower transition state (TS). The formation energy of CO<sub>2</sub> on the Pt<sub>1</sub>/CeO<sub>2</sub>@CeO<sub>2</sub> samples was -1.29 eV. The formation energy of CO<sub>2</sub> on the Pt<sub>1</sub>/CeO<sub>2</sub> samples was -1.36 eV (Fig. 4h). It indicated that CO was more easily converted to CO<sub>2</sub> over the Pt<sub>1</sub>/CeO<sub>2</sub>@CeO<sub>2</sub> samples.



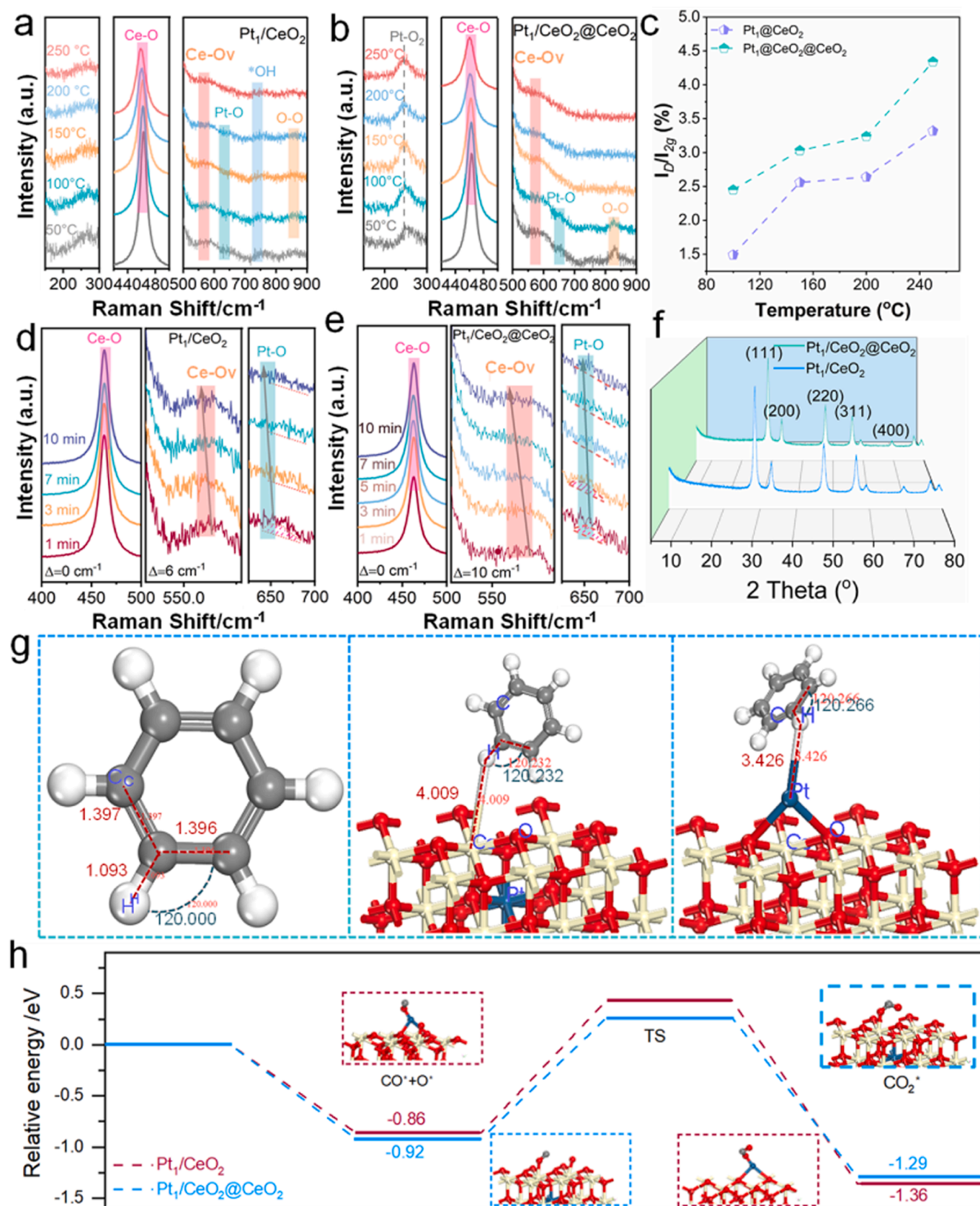


**Fig. 4.** In situ SERS of benzene adsorption at different temperatures over (a)  $\text{Pt}_1/\text{CeO}_2$  and (b)  $\text{Pt}_1/\text{CeO}_2@ \text{CeO}_2-0.1$  Samples, (c) the image of  $I_{\text{D}}/I_{2\text{g}}$  at different temperatures, (d) In situ SERS of benzene adsorption at 50 °C for different times over  $\text{Pt}_1/\text{CeO}_2$  samples, (e) In situ SERS of benzene adsorption at 50 °C for different times over  $\text{Pt}_1/\text{CeO}_2@ \text{CeO}_2-0.1$  samples, (f) XRD patterns of the  $\text{Pt}_1/\text{CeO}_2$  and  $\text{Pt}_1/\text{CeO}_2@ \text{CeO}_2-0.1$  samples, the adsorption images of benzene over  $\text{Pt}_1/\text{CeO}_2$  and  $\text{Pt}_1/\text{CeO}_2@ \text{CeO}_2-0.1$  samples, (g) the relative energy of the absorbed CO over  $\text{Pt}_1/\text{CeO}_2$  and (h)  $\text{Pt}_1/\text{CeO}_2@ \text{CeO}_2-0.1$  samples and the generating energy of  $\text{CO}_2$  over  $\text{Pt}_1/\text{CeO}_2$  and  $\text{Pt}_1/\text{CeO}_2@ \text{CeO}_2-0.1$  samples.

XPS was used to evaluate the surface element states of the catalyst. Fig. S5a showed the fine maps of Ce 3d [41,42]. The content of  $\text{Ce}^{3+}$  species was listed in Table S2. It followed the order:  $\text{Pt}_1/\text{CeO}_2 @\text{CeO}_2-0.4$  (23.92%) >  $\text{Pt}_1/\text{CeO}_2 @\text{CeO}_2-0.2$  (23.08%) >  $\text{Pt}_1/\text{CeO}_2 @\text{CeO}_2-0.1$  (22.98%) >  $\text{Pt}_1/\text{CeO}_2 @\text{CeO}_2-0.02$  (22.36%) >  $\text{Pt}_1/\text{CeO}_2$  (19.49%). With the  $\text{CeO}_2$  cage thicker, the ratio of  $\text{Ce}^{3+}$  species had a significant increase. It indicated that the addition of  $\text{CeO}_2$  could effectively change the coordination environment of Pt SA. In general, more  $\text{Ce}^{3+}$  species would lead more surface oxygen vacancies. Oxygen vacancies were often used to fix Pt SA. In this way, the  $\text{CeO}_2$  cage could effectively restrict the agglomeration of Pt atoms during calcination. Because of the low loading amount of Pt, the valence of Pt wasn't

detected on the surface of these samples (Fig. S6a).

### 3.5. The oxygen mobility analysis

Fig. 5a showed the fine maps of O 1s. The spectrum of O 1s was fitted to 3 peaks [43,44]. From the surface states of O element (Table S2 and Fig. 5e), it could be found that  $\text{O}_\alpha$  had a significant increase and shift. The increased  $\text{O}_\alpha$  might come from the  $\text{CeO}_2$  cage and Pt-O bond. According to Fig. 5a, the lattice oxygen species in the  $\text{Pt}_1/\text{CeO}_2 @\text{CeO}_2-x$  samples shifted to higher binding energy. It meant that more electrons transferred from lattice oxygen to active metal. So the interactions between atoms were enhanced. From the in-situ SERS result, the enhanced

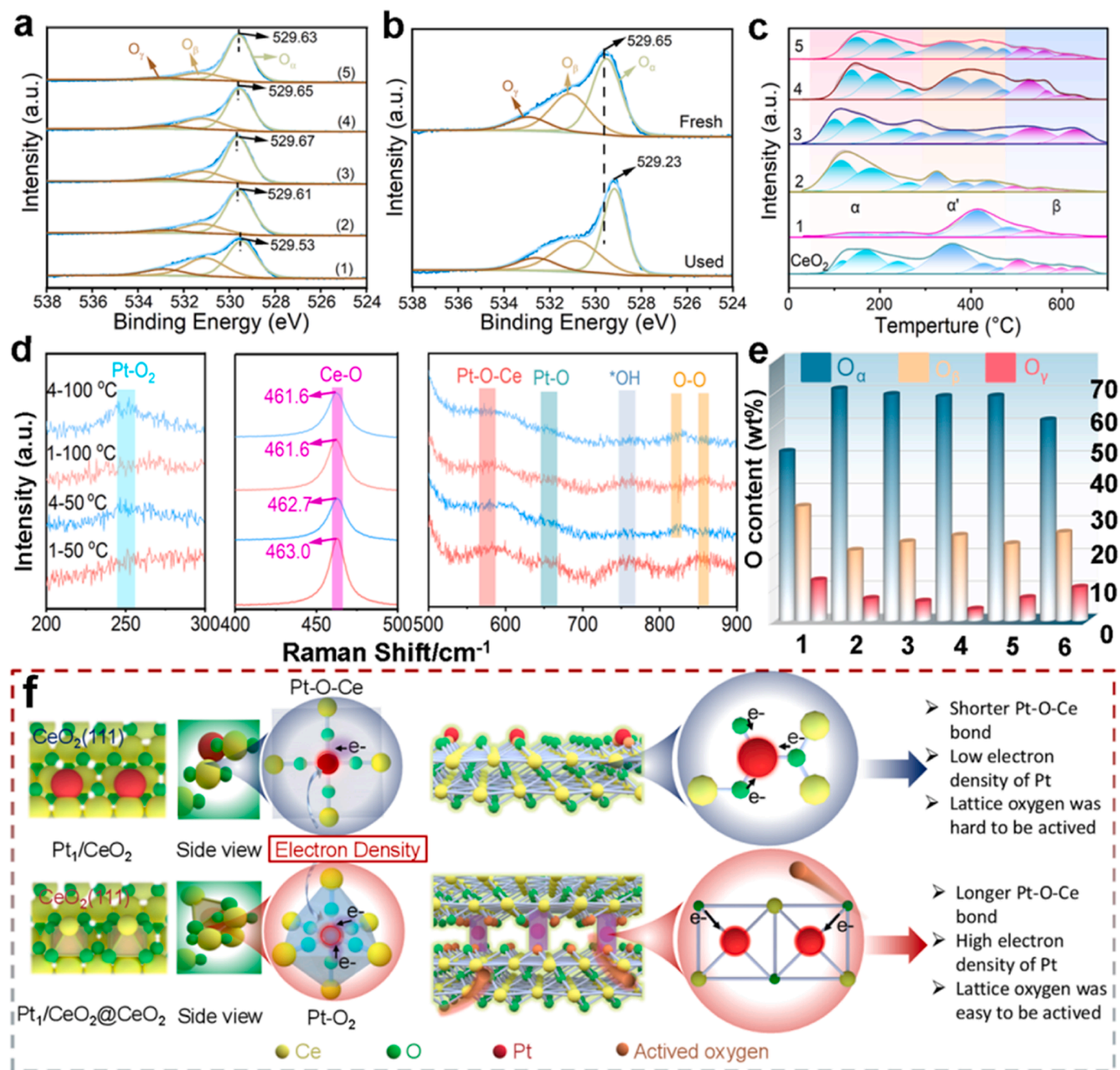


**Fig. 5.** (a) XPS O 1s spectra by XPS, (b) XPS O 1s spectra of the fresh and used  $\text{Pt}_1/\text{CeO}_2 @\text{CeO}_2-0.1$  samples, (c)  $\text{O}_2$ -TPD curves, (d) In situ SERS at different temperatures over  $\text{Pt}_1/\text{CeO}_2$  (1) and  $\text{Pt}_1/\text{CeO}_2 @\text{CeO}_2-0.1$  (4) Samples, (e) the content of O species, and (f) the process of oxygen activation over  $\text{Pt}_1/\text{CeO}_2$  and  $\text{Pt}_1/\text{CeO}_2 @\text{CeO}_2-0.1$  Samples. In this figure, (1) is  $\text{Pt}_1/\text{CeO}_2$ , (2) is  $\text{Pt}_1/\text{CeO}_2 @\text{CeO}_2-0.02$ , (3) is  $\text{Pt}_1/\text{CeO}_2 @\text{CeO}_2-0.1$ , (4) is  $\text{Pt}_1/\text{CeO}_2 @\text{CeO}_2-0.2$ , (5) is  $\text{Pt}_1/\text{CeO}_2 @\text{CeO}_2-0.4$  and (6) is used- $\text{Pt}_1/\text{CeO}_2 @\text{CeO}_2-0.1$  samples.



$O_{\alpha}$  might come from the Pt-O and Pt-O<sub>2</sub> bond. The  $O_{\alpha}$  amount of the used Pt<sub>1</sub>/CeO<sub>2</sub> @CeO<sub>2</sub>-0.2 catalyst also had an obvious decrease (Fig. 5b). This might be caused that the benzene or toluene molecules were absorbed on the surface of the catalyst first. And then the absorbed molecules reacted with lattice oxygen. As a result of this, the amount of lattice oxygen decreased. It meant that  $O_{\alpha}$  might be consumed in the catalytic combustion of VOCs (Fig. 5f). It turned out that  $O_{\alpha}$  played an important role.

As shown in Fig. 5c, peaks below 300 °C were regarded as surface adsorbed oxygen ( $\alpha$ ), which was mainly absorbed at surface oxygen vacancies. Peaks between 300 and 500 °C were regarded as surface

lattice oxygen ( $\alpha'$ ), which was mainly absorbed at lattice defects. Peaks above 500 °C were regarded as bulk lattice oxygen ( $\beta$ ) [45,46]. The CeO<sub>2</sub> support showed abundant surface adsorbed oxygen ( $\alpha$ ) and surface lattice oxygen ( $\alpha'$ ), which could be used to fix Pt SA. With the formation of Pt SA,  $\alpha$  had a significant decrease and  $\alpha'$  had a significant increase (Pt<sub>1</sub>/CeO<sub>2</sub>), which meant the formation of Pt-O bond. With the construction of CeO<sub>2</sub> cage, surface lattice oxygen ( $\alpha'$ ) had a significant increase (Pt<sub>1</sub>/CeO<sub>2</sub> @CeO<sub>2</sub>-0.02). With the cage thicker and thicker, the ratio of  $\alpha'$  had an obvious increase (Table S3). This meant more oxygen was absorbed on the lattice defects of Pt-O bond and the Pt-O<sub>2</sub> bond was formed. The increased  $\alpha$  and  $\alpha'$  also meant the improvement of oxygen

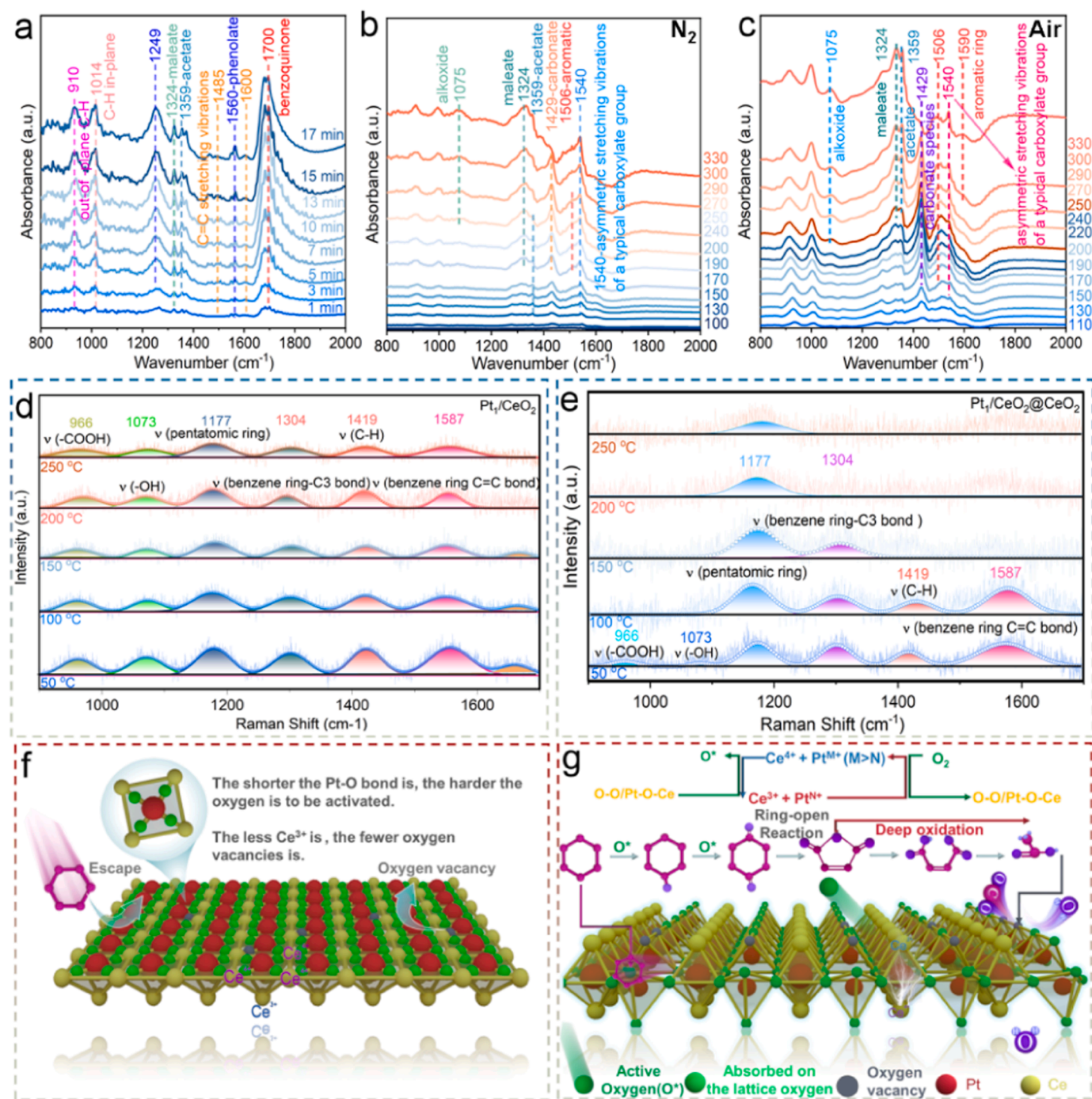


**Fig. 6.** (a) In situ DRIFTS spectra of benzene adsorption at 100 °C, In situ DRIFTS spectra of Pt<sub>1</sub>/CeO<sub>2</sub> @CeO<sub>2</sub>-0.1 catalyst at different temperature under the flow of (b) N<sub>2</sub> and (c) air, In situ SERS spectra over the (d) Pt<sub>1</sub>/CeO<sub>2</sub> and (e) Pt<sub>1</sub>/CeO<sub>2</sub> @CeO<sub>2</sub>-0.1 samples between 900 and 1700 cm<sup>-1</sup>, (f) the proposed reaction mechanisms over Pt<sub>1</sub>/CeO<sub>2</sub> and Pt<sub>1</sub>/CeO<sub>2</sub> @CeO<sub>2</sub>-0.1 samples.



mobility.

Fig. 5d and Fig. S12 showed the comparison of the Pt<sub>1</sub>/CeO<sub>2</sub> and Pt<sub>1</sub>/CeO<sub>2</sub>@CeO<sub>2</sub>-0.1 samples in in-situ SERS. It could be found that the Pt<sub>1</sub>/CeO<sub>2</sub>@CeO<sub>2</sub>-0.1 samples showed stronger Pt-O<sub>2</sub> bond. Compared with the Pt<sub>1</sub>/CeO<sub>2</sub> samples, Ce-O bond in the Pt<sub>1</sub>/CeO<sub>2</sub>@CeO<sub>2</sub> samples also shifted to low wavenumber. It meant a higher activity. In the XPS spectrum, Ce 3d also shifted to a high binding energy. It meant more electrons transferred from Ce to lattice oxygen. Between 500 and 900 cm<sup>-1</sup>, Pt<sub>1</sub>/CeO<sub>2</sub> samples showed stronger Pt-O-Ce bond and poor O-O bond. From the O<sub>2</sub>-TPD result, it could be found that oxygen species mainly existed in the form of lattice oxygen, which limited the oxygen mobility. And it also showed a stronger \*OH bond, which was accordance with the O 1s spectrum. The Pt<sub>1</sub>/CeO<sub>2</sub> samples had more water or hydroxyl molecules (O<sub>1</sub>).

### 3.6. Possible catalytic reaction pathways

In situ DRIFTS were used to study the role of oxygen species, the reaction mechanism and the important intermediates in the benzene oxidation over the 3DOM Pt<sub>1</sub>/CeO<sub>2</sub>@CeO<sub>2</sub>-0.1 samples under benzene/N<sub>2</sub> flow. Fig. 6a showed the adsorption of benzene over the Pt<sub>1</sub>/CeO<sub>2</sub>@CeO<sub>2</sub>-0.1 samples. Peaks at 1600, 1485, and 1324 cm<sup>-1</sup> could be regarded as the C=C stretching vibrations of aromatic rings [47,48]. It illustrated that benzene adsorbed on the surface successfully. Then the adsorbed benzene reacted with the active oxygen species to form the phenolate species (1249 and 1560 cm<sup>-1</sup>). With the adsorption time increasing, the phenolate species were deeply oxidized to the benzoquinone species (1414 and 1727 cm<sup>-1</sup>), maleate (1324 cm<sup>-1</sup>) and the acetate species (1357 cm<sup>-1</sup>) [49,50]. It illustrated that the active oxygen species participated in the ring-opening reaction and the smaller intermediates (such as acetate species) formed. From this, it could be found that the conversion of benzene might follow the order: phenol, benzoquinone, maleate, and acetate species. From this, it could be concluded that the active species played an important role on the combustion of benzene. Peaks at 910 and 1014 cm<sup>-1</sup> could be regarded as the C-H in-plane bending vibration and the C-H out-of-plane bending vibration. Fig. 6b and S10 showed the temperature-dependent DRIFTS spectra over the 3DOM Pt<sub>1</sub>/CeO<sub>2</sub>@CeO<sub>2</sub>-0.1 samples under the N<sub>2</sub> flow. It was found that the surface intermediates changed significantly with the temperature increasing. The characteristic peaks represented as phenol and benzoquinone disappeared. It might illustrate that the species was easily oxidized. The characteristic peaks represented as the aromatic ring (1506 cm<sup>-1</sup>) also disappeared when the temperature increased to 290 °C. This illustrated that the ring was broken and the deep oxidation reaction happened. Similar with this, the characteristic peaks represented as acetate (1359 cm<sup>-1</sup>) gradually increased and eventually disappeared when the temperature increased to 270 °C. It might illustrate that the acetate species was preferentially converted to CO<sub>2</sub> and H<sub>2</sub>O. The intensity of peaks at 1429 and 1075 cm<sup>-1</sup> gradually increased, which could be regarded as the asymmetric stretching vibrations of a typical carboxylate group (C=O) and alkoxide (C-O), respectively. This meant the formation of maleate (1324 cm<sup>-1</sup>) [51,52]. Above all, it could be found that the lattice oxygen participated in the oxidation reaction. To study the influence of oxygen species on the oxidation of benzene, the temperature-dependent DRIFTS spectra over the 3DOM Pt<sub>1</sub>/CeO<sub>2</sub>@CeO<sub>2</sub>-0.1 samples under the air flow (Fig. 6c and Fig. S11). Compared with the result under the N<sub>2</sub> flow, the intensity of peaks at 1359 cm<sup>-1</sup> gradually increased. And peaks at 1075 and 1540 cm<sup>-1</sup> weakened. It meant that maleate species were consumed and more acetate species were generated. This illustrated that the introduction of O<sub>2</sub> accelerated the conversion from the maleate species to acetate species. From this, it might be concluded that the absorbed oxygen species was beneficial for the deep oxidation. But it could be also found that the characteristic peaks represented as aromatic ring gradually strengthened when the temperature increased to 330 °C. This might be related to the consumption of maleate. Above all, it could be

found that the lattice oxygen participated in the oxidation reaction and the absorbed oxygen species accelerated this reaction.

To further study the influence of oxygen species on the oxidation of benzene, in-situ SERS were conducted on the Pt<sub>1</sub>/CeO<sub>2</sub> and Pt<sub>1</sub>/CeO<sub>2</sub>@CeO<sub>2</sub>-0.1 samples under the air flow (Fig. 6d and e). The peaks at 966 and 1073 cm<sup>-1</sup> could be regarded as the stretching vibrations of -OH and -COOH. The peaks at 1177 cm<sup>-1</sup> and 1304 cm<sup>-1</sup> could be regarded as the stretching vibrations of pentatomic ring and benzenering-C3 bond, respectively. The peaks at 1419 cm<sup>-1</sup> could be regarded as the stretching vibrations of C-H. The peaks at 1549 cm<sup>-1</sup> and 1587 cm<sup>-1</sup> could be regarded as the stretching vibrations of benzene ring C=C bond. The temperature-dependent SERS spectra showed that the intermediates over the Pt<sub>1</sub>/CeO<sub>2</sub> samples didn't have too much difference with the temperature increasing. While the intermediates over the Pt<sub>1</sub>/CeO<sub>2</sub>@CeO<sub>2</sub>-0.1 samples had a significant change. The characteristic peaks represented as the -OH, -COOH, benzenering-C3 bond, C-H, and benzene ring C=C bond gradually weakened and disappeared. And the characteristic peaks represented as the pentatomic ring existed. With the temperature increasing, the O-O bond gradually weakened. It indicated that benzene was first absorbed on the O species and then was activated. The enhanced Pt-O<sub>2</sub> bond meant that high temperatures made more oxygen molecules absorb on the surface. It might illustrate that the oxygen mobility was improved. This might illustrate that why the Pt<sub>1</sub>/CeO<sub>2</sub>@CeO<sub>2</sub>-0.1 samples had a better catalytic activity.

Combined with the result of in-situ DRIFTS, it could be found that the lattice oxygen was beneficial for the ring-open reaction (Fig. 6f and g). From the H<sub>2</sub>-TPR result, it could be found that the reduction peaks shifted to a low temperature with the construction of CeO<sub>2</sub> cage. This meant that the construction of CeO<sub>2</sub> cage led a more active Pt-O bond and better reduction ability. According to the O<sub>2</sub>-TPD result, the Pt<sub>1</sub>/CeO<sub>2</sub>@CeO<sub>2</sub>-0.1 samples showed more surface adsorbed oxygen. According to the XPS result, it could be found that the lattice oxygen species had a significant increase and shift. It meant that more electrons transferred from lattice oxygen to active metal. The interactions between atoms enhanced. Based on the in situ SERS results, it could be confirmed that the Pt<sub>1</sub>/CeO<sub>2</sub>@CeO<sub>2</sub>-0.1 samples showed stronger Pt-O<sub>2</sub> bond. This might illustrate that the lattice oxygen over the Pt<sub>1</sub>/CeO<sub>2</sub>@CeO<sub>2</sub>-0.1 samples was more likely to be activated than the Pt<sub>1</sub>/CeO<sub>2</sub> samples. From the above analysis, it was also found that the M-O bonds over Pt<sub>1</sub>/CeO<sub>2</sub>@CeO<sub>2</sub>-0.1 samples were easily broken and it also had abundant peroxy or superoxy species. These also confirmed that the Pt<sub>1</sub>/CeO<sub>2</sub>@CeO<sub>2</sub>-0.1 samples had more active oxygen species and better activity.

## 4. Conclusions

In conclusion, via dual nanospace confinement of CeO<sub>2</sub> pore and Ce-MOFs nanocages, the chemical environment of Pt SA was successfully changed and more active lattice oxygen linked to Pt SA. During calcination, CeO<sub>2</sub> derived from Ce-MOF restricted the migration of Pt SA and prevented the agglomeration of Pt SA. With the construction of CeO<sub>2</sub> nanocage, the in-situ SERS result confirmed that more active Pt-O<sub>2</sub> bond was created. By varying the thickness of CeO<sub>2</sub> nanocage, the catalytic performance and chemical properties of the catalyst was obviously improved. With CeO<sub>2</sub> nanocage thicker, the ratio of Ce<sup>3+</sup> and O<sub>1s</sub> had a significant increase. This was beneficial for the anchoring of Pt SA. According to the XPS and in-situ SERS result, it could be found that more surface lattice oxygen was active. The characterizations also confirmed that the metal-support interaction and active lattice oxygen have been significantly improved. With the proper thickness of CeO<sub>2</sub> nanocage, the Pt<sub>1</sub>/CeO<sub>2</sub>@CeO<sub>2</sub>-0.2 samples had the best catalytic performance. The T<sub>90</sub> has been reduced by 80 °C in the catalytic combustion of benzene and by 60 °C in the catalytic combustion of toluene. The intermediates and reaction path were carefully studied with the help of in-situ SERS and in-situ DRIFTS. It followed this order: phenol, benzoquinone and carboxylate species. The DFT calculations also confirmed that benzene

was easily absorbed and activated over the Pt<sub>1</sub>/CeO<sub>2</sub> @CeO<sub>2</sub> samples. And CO was more easily oxidized to CO<sub>2</sub>. It is illustrated that the construction of CeO<sub>2</sub> nanocage could create more active interface and the precise control of Pt SA could improve the catalytic performance. This work opened a new door to tune the local chemical environments of SACs for more applications in other reactions.

### Declaration of Competing Interest

The authors declare that they have no known competing financial interests or personal relationships that could have appeared to influence the work reported in this paper.

### Data Availability

The authors do not have permission to share data.

### Acknowledgements

This work was supported by the National Natural Science Foundation of China (52070182), Province Natural Science Foundation of GanSu (23JRRA638, 23JRRA622), the DNL Cooperation Found, CAS (DNL202004), the Joint Fund of the Yulin University and the Dalian National Laboratory for Clean Energy (YLU-DNL Fund 202206), Talents of Innovation and Entrepreneurship Project of Lanzhou, China (2022-RC-26), Major Program of the Lanzhou Institute of Chemical Physics, CAS (No. ZYFZFX-10).

### Appendix A. Supporting information

Supplementary data associated with this article can be found in the online version at [doi:10.1016/j.apcatb.2023.123687](https://doi.org/10.1016/j.apcatb.2023.123687).

### References

- [1] F. Jiang, Z. Zhou, C. Zhang, C. Feng, G. Xiong, Y. Wang, Z. Fei, Y. Liu, Y. Pan, *Nano Res.* 16 (2023) 1967–1983.
- [2] W. Qu, S. Niu, D. Sun, H. Gao, Y. Wu, Z. Yuan, X. Chen, Y. Wang, T. An, G. Wang, F. Zhao, *Adv. Sci.* 8 (2021) 2002889.
- [3] B. Wang, Q. Yang, B. Li, H. Ma, Y. Xuan, C. Gao, Y. Liang, K. Zhang, Q. Chang, O. Broesicked, H. Wang, D. Wang, T. Luan, K. Han, C. Lu, J. Crittenden, *Appl. Catal. B: Environ.* 332 (2023) 122753.
- [4] Y. Su, K. Fu, Y. Zheng, N. Ji, C. Song, D. Ma, X. Lu, R. Han, Q. Liu, *Appl. Catal. B: Environ.* 288 (2021) 119980.
- [5] F. Bi, Z. Zhao, Y. Yang, W. Gao, N. Liu, Y. Huang, X. Zhang, *Environ. Sci. Technol.* 56 (2022) 17321–17330.
- [6] P. Yin, Q. Yan, H. Liang, *Angew. Chem. Int. Ed.* (2023) e202302819.
- [7] J. Yu, A. Muhetaer, X. Gao, Z. Zhang, Y. Yang, Q. Li, L. Chen, H. Liu, D. Xu, *Angew. Chem. Int. Ed.* (2023) e202303135.
- [8] H. Zhang, S. Hwang, M. Wang, Z. Feng, S. Karakalos, L. Luo, Z. Qiao, X. Xie, C. Wang, D. Su, Y. Shao, G. Wu, *J. Am. Chem. Soc.* 139 (2017) 14143–14149.
- [9] Y. Tang, Y. Wei, Z. Wang, S. Zhang, Y. Li, L. Nguyen, Y. Li, Y. Zhou, W. Shen, F. Tao, P. Hu, *J. Am. Chem. Soc.* 141 (2019) 7283–7293.
- [10] Q. Mo, L. Zhang, S. Li, H. Song, Y. Fan, C. Su, *J. Am. Chem. Soc.* 144 (2022) 22747–22758.
- [11] H. Wang, X. Liu, W. Yang, G. Mao, Z. Meng, Z. Wu, H. Jiang, *J. Am. Chem. Soc.* 144 (2022) 22008–22017.
- [12] Q. Fu, W. Li, Y. Yao, H. Liu, H. Su, D. Ma, X. Gu, L. Chen, Z. Wang, H. Zhang, B. Wang, X. Bao, *Science* 328 (2010) 1141–1144.
- [13] J. Kim, D. Shin, J. Lee, D. Baek, T. Shin, Y. Kim, H. Jeong, J. Kwak, H. Kim, S. Joo, *ACS Nano* 14 (2020) 1990–2001.
- [14] Z. Jiang, M. Jing, X. Feng, J. Xiong, C. He, M. Douthwaite, L. Zheng, W. Song, J. Liu, Z. Qu, *Appl. Catal. B: Environ.* 278 (2020) 119304.
- [15] B. Han, Y. Guo, Y. Huang, W. Xi, J. Xu, J. Luo, H. Qi, Y. Ren, X. Liu, B. Qiao, T. Zhang, *Angew. Chem. Int. Ed.* 59 (2020) 11824–11829.
- [16] X. Yu, Z. Zhao, Y. Wei, J. Liu, *Sci. Rep.* 7 (2016) 43894.
- [17] K. Yang, Y. Liu, J. Deng, X. Zhao, J. Yang, Z. Han, Z. Hou, H. Dai, *Appl. Catal. B: Environ.* 244 (2019) 650–659.
- [18] B. Ravel, M. Newville, *J. Synchrotron Radiat.* 12 (2005) 537–541.
- [19] S. Zabinsky, J. Rehr, A. Ankudinov, *Phys. Rev. B* 52 (1995) 2995–3009.
- [20] M. Su, J. Dong, J. Le, Y. Zhao, W. Yang, Z. Yang, G. Attard, G. Liu, J. Cheng, Y. Wei, Z. Tian, J. Li, *Angew. Chem. Int. Ed.* 59 (2020) 23554–23558.
- [21] M. Liang, Y. Wang, R. Shao, W. Yang, H. Zhang, Hua Zhang, Z. Yang, J. Li, Z. Tian, *Electrochem. Commun.* 81 (2017) 38–42.
- [22] A. Zhang, Z. Zhang, H. Lu, Z. Liu, J. Xiang, C. Zhou, W. Xing, L. Sun, *Ind. Eng. Chem. Res.* 54 (2015) 2930–2939.
- [23] D. Yang, F. Dong, W. Han, J. Zhang, Z. Tang, *ACS Appl. Mater. Interfaces* 15 (2023) 42541–42556.
- [24] Y. Zhang, C. Wu, Z. Wang, J. Jia, H. Wan, W. Zou, Q. Tong, J. Sun, Lin Dong, Y. Chen, *Appl. Surf. Sci.* 580 (2022) 152278.
- [25] S. Zhao, K. Li, S. Jiang, J. Li, *Appl. Catal. B: Environ.* 181 (2016) 236–248.
- [26] M. Wen, F. Dong, J. Yao, Z. Tang, J. Zhang, *J. Catal.* 412 (2022) 42–58.
- [27] J. Fan, Y. Sun, M. Fu, J. Li, D. Ye, *J. Hazard. Mater.* 424 (2022) 127505.
- [28] D. Chen, Z. Wang, Z. Li, Y. Zhu, *Microporous Mesoporous Mat.* 350 (2023) 112464.
- [29] K. Ren, X. Zhao, J. Zhong, J. Zhang, J. Tian, D. Yan, P. Liu, M. Fu, L. Chen, J. Wu, D. Ye, *J. Catal.* 418 (2023) 130–140.
- [30] B. Hu, M. Li, Z. Zhang, Y. Zhu, *Appl. Catal. A, Gen.* 650 (2023) 118999.
- [31] M. Wang, D. Chen, N. Li, Q. Xu, H. Li, J. He, J. Lu, *Small* 16 (2020) 2005715.
- [32] M. Xiao, X. Yu, Y. Guo, M. Ge, *Environ. Sci. Technol.* 56 (2022) 1376–1385.
- [33] J. Zhang, C. Rao, H. Peng, C. Peng, L. Zhang, X. Xu, W. Liu, Z. Wang, N. Zhang, X. Wang, *Chem. Eng. J.* 334 (2018) 10–18.
- [34] B. Wang, B. Chen, Y. Sun, H. Xiao, X. Xu, M. Fu, J. Wu, L. Chen, D. Ye, *Appl. Catal. B: Environ.* 238 (2018) 328–338.
- [35] J. Yang, Y. Huang, H. Qi, C. Zeng, Q. Jiang, Y. Cui, Y. Su, X. Du, X. Pan, X. Liu, W. Li, B. Qiao, A. Wang, T. Zhang, *Nat. Commun.* 13 (2022) 4244.
- [36] L. Yang, Q. Liu, R. Han, K. Fu, Y. Su, Y. Zheng, X. Wu, C. Song, N. Jia, X. Lu, D. Ma, *Appl. Catal. B: Environ.* 309 (2022) 121224.
- [37] Y. Huang, P. Kooyman, M. Koper, *Nat. Commun.* 7 (2016) 12440.
- [38] Wang, X. Shi, L. Chen, H. Li, M. Mao, G. Zhang, H. Yi, M. Fu, D. Ye, J. Wu, *Appl. Catal. A: Gen.* 625 (2021) 118342.
- [39] F. Wang, P. Wang, T. Lan, Y. Shen, W. Ren, D. Zhang, *ACS Catal.* 12 (2022) 7622–7632.
- [40] D. Wei, M. Yue, S. Qin, S. Zhang, Y. Wu, G. Xu, H. Zhang, Z. Tian, J. Li, *J. Am. Chem. Soc.* 143 (2021) 15635–15643.
- [41] Z. Cai, G. Zhang, Z. Tang, J. Zhang, *Nanoscale* 14 (2022) 12281.
- [42] M. Wen, F. Dong, Z. Tang, J. Zhang, *Mol. Catal.* 519 (2022) 112149.
- [43] M. Wen, F. Dong, J. Yao, Z. Tang, J. Zhang, *J. Catal.* 412 (2022) 42–58.
- [44] X. Du, F. Dong, Z. Tang, J. Zhang, *Nanoscale* 12 (2020) 12133–12145.
- [45] K. Xu, R. Zhou, K. Takei, M. Hong, *Adv. Sci.* 6 (2019) 1900925.
- [46] X. Yu, L. Wang, M. Chen, X. Fan, Z. Zhao, K. Cheng, Y. Chen, Z. Sojka, Y. Wei, J. Liu, *Appl. Catal. B: Environ.* 254 (2019) 246–259.
- [47] Y. Wang, J. Wu, G. Wang, D. Yang, T. Ishihara, L. Guo, *Appl. Catal. B: Environ.* 285 (2021) 119873.
- [48] X. Wang, Y. Liu, T. Zhang, Y. Luo, Z. Lan, K. Zhang, J. Zuo, L. Jiang, R. Wang, *ACS Catal.* 7 (2017) 1626–1636.
- [49] X. Wang, Y. Liu, T. Zhang, Y. Luo, Z. Lan, K. Zhang, J. Zuo, L. Jiang, R. Wang, *ACS Catal.* 7 (2017) 1626–1636.
- [50] E. Yang, Z. Su, Z. Xu, W. Yang, Y. Peng, J. Li, *Appl. Catal. B: Environ.* 260 (2020) 118150.
- [51] F. Dong, W. Han, Y. Guo, W. Han, Z. Tang, *Chem. Eng. J.* 405 (2021) 126948.
- [52] Y. Wang, J. Wu, G. Wang, D. Yang, T. Ishihara, L. Guo, *Appl. Catal. B: Environ.* 285 (2021) 119873.